CHAPTER 3

Experimental aparatus and analysis tools

3.1 Output characteristics of lasers and pulse shaping aparatus

3.1.1 Radiation sources

The femtosecond source used for the adaptive pulse shaping experiments is a Ti:Sapphire system (Quantronix) based on the Chirped-Pulse-Amplification technique. It is referred to as system I all along this thesis. This system includes a self mode-locked oscillator pumped by a continuous Ar+ laser that delivers 100 fs pulses at a repetition rate of 82 MHz. The output pulses are stretched up to 100 ps in a homemade diffraction-grating-based stretching unit and seed a regenerative amplifier. The active medium of the regenerative amplifier is a Ti:Sapphire crystal pumped by a 7W Nd:YLF pump laser. Amplified pulses with a bandwidth of approximately 7 nm are extracted out of the amplifier cavity by a Pockels cell, allowing flexible user-selectable repetition rates from 100 Hz up to 1 kHz. Working at low repetition rates allows for the additional use of an electromechanical shutter (Uniblitz) to pick out individual pulses and therefore decrease the nominal repetition rate. The compressor is basically a mirrored setup of the stretcher. It conveniently allows to tune the amount of chirp carried by the pulse at the output of the system. The chirp amount can be arbitrarily fixed by simple translation of a diffraction grating, without noticeable shift of the propagation axis. On demand, this chirp can be negative (spectral components of higher frequencies

come first), positive (natural dispersion-like) or canceled (shortest pulse). The shortest pulse duration available is about 200 fs and the maximum energy per pulse about 400 μJ. The beam is linearly polarized and has a diameter of about 3 mm. In the time domain, pulses are assumed to be gaussian with a contrast between the main pulse and the background better than 10^3. This system is equipped with a temporal pulse shaping apparatus.

For the time-resolved pictures, a laser system (system II) with a higher energy per pulse and shorter pulse duration (Clark OCR-1000) has been preferred, also based on a CPA technique. Both amplifier and oscillator use a Ti:Sapphire as an active medium, delivering femtosecond light wave packets with very similar spectral characteristics as system I. The repetition rate is controllable via the Pockels cell driving from 166 Hz to 1kHz. The lowest repetition rate allows to use an additional electromechanical shutter in order to pick up single pulses or reduce the repetition rate to the user convenience. The available amount of energy per pulse is about 600 μJ. The pulse duration, measured with a commercially available autocorrelator (APE PulseCheck Autocorrelator), is estimated to be 90 fs. We also used a Spectra Physics Spitfire system (system III) for some time-resolved pictures. The main characteristics of this system are: a short pulse duration (about 50fs) and a high energy per pulse (up to 1.5 mJ). Similarly to the other laser sources, it has been employed at a low repetition rate (166 Hz) in combination with an electromechanical shutter.

Finally, the high repetition rate system used to carry out the writing of buried optical functions in the bulk of transparent materials is a system including a Vitesse oscillator (Coherent) and a RegA amplifier (Coherent) also based on a CPA technique. Those two lasers rely on Ti:Sapphire active media and produce pulses with 13 nm FWHM spectra centered around 800 nm. Both are pumped by a continuous wave laser delivering 10 W. About 20% of the output power is used to pump the oscillator and the rest feeds the regenerative amplifier. This system is designed to work at high repetition rates. A pair of acousto-optic modulators is used for the injection and extraction of the pulses and for Q-switching the cavity. The repetition rate is easily tunable over a range from 10 to 250 kHz. The final energy per pulse being about 4 μJ, it is not necessary to stretch the seed pulses prior to amplification since intrinsic dispersion is considered. The group velocity dispersion in the active medium of the amplifier and in the acousto-optic modulators is sufficient to increase the pulse duration up to 20 ps and to avoid any risk of damaging the cavity mirrors. The amplified pulse is then dispersion-corrected with the help of a compressor based on a single dispersion grating system. Pulses as short as 130 fs are delivered. The output beam has a diameter of about 4.5 mm. This system is also equipped with a temporal pulse shaping apparatus.

Table 3.1 shows a summary of the main characteristics of the output pulses for the different lasers.

Table 3.1: Main characteristics of the output pulses for the different lasers

	System I	System II	System III	System IV
Wavelength (nm)	800	800	800	800
Pulse duration (fs)	200	90	50	130
E_{max} per pulse (μJ)	400	600	1500	4
Repetition rate (kHz)	0.1-1	0.166-1	0.166	10-250
Pulse shaping apparatus	Yes	No	No	Yes

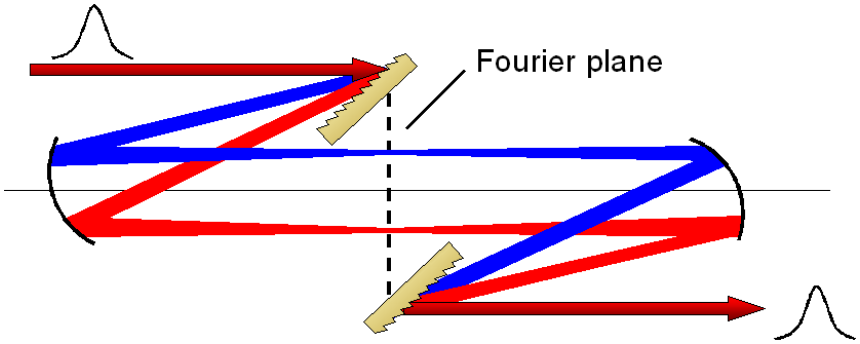

Figure 3.1: Structure of a zero dispersion stretcher unit.

3.1.2 Pulse shaping apparatus

General principles

Temporal pulse shaping is a generic term applicable to any apparatus able to modify the temporal profile of a propagating electromagnetic wave in a controlled way. While controlling the energy deposition on long timescales is achievable by acting directly in the time domain (e.g. with an electromechanical shutter), designing excitation sequences on a femtosecond-to-picosecond timescale requires to intervene in the spectral domain of the incident electric field. A conventional mean to achieve this goal is to alter selectively the optical path of the different spectral components constituting the initial femtosecond pulse.

A pulse shaping unit is basically composed of a mask inserted in the Fourier plane of a zero-dispersion stretcher unit. The principle of such a device is depicted in Fig. 3.1. It is composed of a pair of cylindrical mirrors and a pair of diffraction gratings in a 4f configuration. The first dispersion grating, situated in the rear focal plane of a cylindrical mirror, spectrally decomposes the incoming pulse in a parallel beam. When reaching the front focal plane of the first mirror (i.e. the Fourier plane), the different spectral components are well discriminated in a direction perpendicular to the propagation axis and have minimum waists. The spectral components are recomposed by a mirrored setup. In the absence of a

phase mask in the Fourier plane, a zero dispersion stretcher unit gives an output pulse strictly identical to the input pulse. A phase mask offers the possibility to manipulate individually the phase, the amplitude, or both phase and amplitude of the different spectral components. The mask can be either fix [56] or dynamic [57] for an improved flexibility of the process.

Theoretical description

Temporal pulse shaping is based on a coherent filtering process. As any filter, it is fully characterized by its temporal response $h(t)$ to a delta function. The expression of the output signal $s(t)$ corresponding to an input $e(t)$ is given by

$$s(t) = e(t) * h(t) = \int_{-\infty}^{+\infty} e(t')h(t-t')dt', \tag{3.1}$$

where $*$ denotes a convolution product. In the spectral domain, the convolution product turns into a simple product and Eq. 3.1 rewrites

$$S(\omega) = E(\omega)H(\omega), \tag{3.2}$$

where ω is the radial frequency, $S(\omega)$, $E(\omega)$ and $H(\omega)$ correspond to the Fourier transform of $s(t)$, $e(t)$ and $h(t)$ respectively. In a general case, $H(\omega)$ is a complex function and writes

$$H(\omega) = R(\omega)e^{-i\Psi(\omega)}. \tag{3.3}$$

As previously shown, a pulse shaping system based on a Fourier synthesis is made of a zero-dispersion unit and a phase-mask. Since the zero-dispersion stretcher provides an output strictly identical to the input, it does not contribute to the transfer function of the system. Hence, $H(\omega)$ depends on the optical characteristics of the mask only. The mask is placed in the Fourier plane of the zero dispersion unit. Therefore, $R(\omega)$ directly corresponds to the transmission coefficient of the mask along the direction where the spectral components are dispersed and $\Psi(\omega)$ corresponds to the phase profile of the mask.

For a given mask transmittance $H(\omega)$, the temporal profile $S(t)$ of the output field is given by the inverse Fourier transform of $S(\omega)$:

$$S(t) = \frac{1}{2\pi}\int S(\omega)e^{i\omega t}d\omega = \frac{1}{2\pi}\int E(\omega)R(\omega)e^{-i\Psi(\omega)}e^{i\omega t}d\omega. \tag{3.4}$$

The measurable envelope of the pulse corresponds to the real part of $S(t)$ while the imaginary part gives the residual chirp. In general, an arbitrary form of the output pulse can be obtained by a synchronous amplitude and phase modulation of the input pulse. When a pulse shaping system is used in a phase-only configuration (for reasons associated with energy

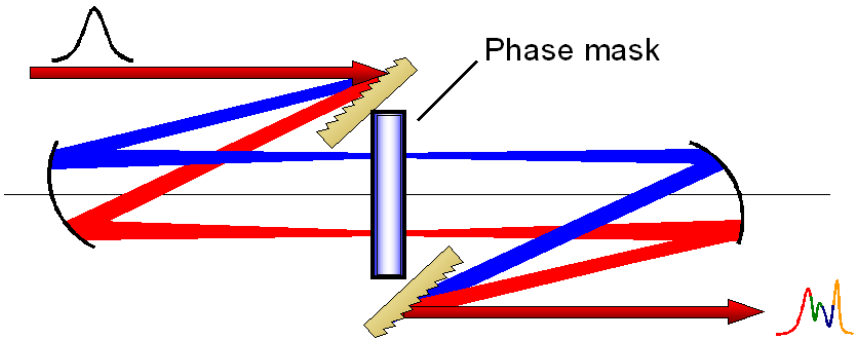

Figure 3.2: Pulse shaping apparatus based on Fourier synthesis of spectral components.

conservation), arbitrary pulse forms can be obtained with a certain degree of approximation. For this purpose, optimization strategies (e.g. Gerchberg-Saxton algorithm) can be used to obtain a satisfactory approximation of the desired pulse.

Practical realization

The pulse shaping apparatus used for the experiments is depicted in Fig. 3.2. Because of chromatic aberrations, mirrors are employed instead of refractive lenses. Cylindrical mirrors are used instead of spherical mirrors in order to minimize the density of energy in the Fourier plane and therefore avoid any risk of damaging the phase mask [58]. The phase mask is a one-dimensional array of liquid crystals comprising 640 pixels (Jenoptik) electrically addressable and allows a phase-only manipulation. This is possible because the geometry of the system enables the variation of the local pixel refractive index (via adequate liquid-crystal rotation) with no associated rotation of polarization. Hence, the energy per pulse stays constant for any programmed temporal shape. The mirrors have a focal distance of 40 cm and diffraction gratings with a period of 2000 lines/mm are used. The resolution is about 0.1 nm per pixel for the Quantronix setup. The pulse shaping unit is inserted between the oscillator and the regenerative amplifier. In this way, the cavity of the regenerative amplifier plays the role of a spatial filter, allowing the delivery of a TEM_{00} beam only. This configuration notably prevents problems of beam distortion that may occur when modifying the spectrum of the beam [59] and regenerates the beam spatially and energetically.

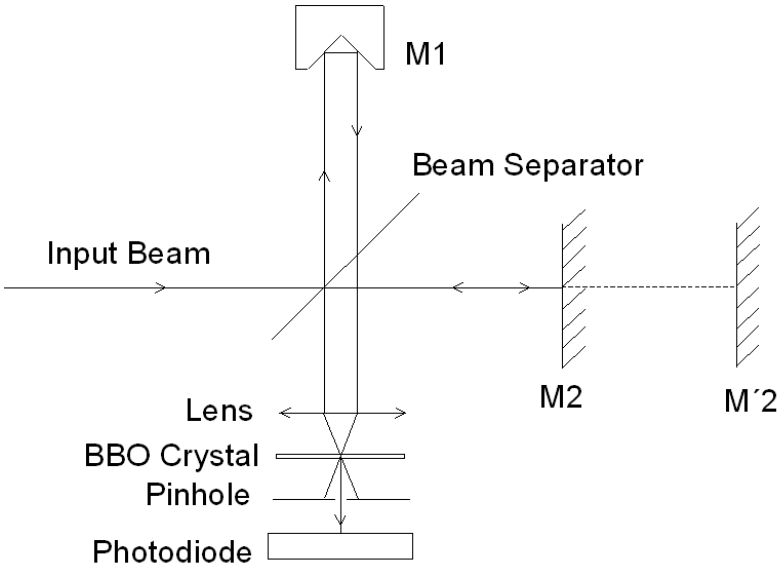

Figure 3.3: Auto/cross-correlation apparatus

3.1.3 Pulse characterization techniques

Basic principles and practical realization

When performing beam shaping, a method for characterizing the temporal profile of the final pulse is needed. For this purpose, we use a homemade interferometric auto/cross-correlator. Such an apparatus is based on a Michelson interferometer as shown in Fig. 3.3. The role of the mirrors M2 and M'2 will be explained at a later point.

When the pulses are reflected back and overlap spatially and temporally into the SHG crystal, a correlation signal $S(\Delta t)$ is detected by the photodiode. An auto/cross-correlation measurement consists of recording the signal delivered by the photodiode for different positions of M1, which translates into a variable relative delay Δt between the correlating pulses ε_1 and ε_2 (ε_1') reflected by M1 and M2 (M'2).

The signal $G(\Delta t)$ delivered by the photodiode for different values of Δt is proportional to:

$$G(\Delta t) \propto \int_{-\infty}^{+\infty} \{[\varepsilon_1 (t - \Delta t) + \varepsilon_2(t)]^2\}^2 dt. \tag{3.5}$$

It corresponds to the interferometric signal resulting from the superposition of ε_1 and ε_2. In a general way, the fields ε_1 and ε_2 can be written under the general form (see Eq. 2.1)

$$\varepsilon(t) = \bar{\varepsilon}(t) e^{i(\omega_l t + \varphi)} \tag{3.6}$$

where $\bar{\varepsilon}(t)$ is the envelope of the field, i.e. the quantity of interest, ω_l is the light radial

frequency, and φ is a phase term. Replacing the expressions of the fields in Eq. 3.5 and expanding the sum, the autocorrelation signal appears as a sum of three waves of frequencies ω_l, $2\omega_l$ and zero. The photodiode being not fast enough for resolving high frequency fields, the oscillating terms do not contribute to the final signal. The zero frequency term $A(\Delta t)$ only can be measured. According to [11], $A(\Delta t)$ reads

$$A(\Delta t) = \int_{-\infty}^{+\infty} \left[\bar{\varepsilon_1}^4(t-\Delta t) + \bar{\varepsilon_2}^4(t) + 4\bar{\varepsilon_1}^2(t-\Delta t)\bar{\varepsilon_2}^2(t)\right] dt. \tag{3.7}$$

The first and second terms of the sum correspond to the relative contributions of the fields ε_1 and ε_2. Because of the geometry of our setup, those three contributions are well discriminated in space and it is easy to select the third term of Eq. 3.7 with the help of a pinhole. After the pinhole, this apparatus reduces to a simple intensity correlation setup:

$$A_c(\Delta t) = 4\int_{-\infty}^{+\infty} \bar{\varepsilon_1}^2(t-\Delta t)\bar{\varepsilon_2}^2(t)dt \propto 4\int_{-\infty}^{+\infty} I_1(t-\Delta t)I_2(t)dt = 4I_c(\Delta t), \tag{3.8}$$

where $I_c(\Delta t)$ corresponds to the signal obtained by an intensity correlation of second order.

Autocorrelation

In the autocorrelation configuration, M2 is flipped up in the beam path. The pulse to characterize is split in two identical wave packets. The photodiode records the autocorrelation signal I_{AC} defined by

$$I_{AC} = \int_{-\infty}^{+\infty} I(t-\Delta t)I(t)dt \tag{3.9}$$

where $I(t)$ corresponds to the intensity profile of the pulse to characterize. Practically, for each position of M1 around the equilibrium position, the signal delivered by the photodiode is sent to a Labview program plotting on line $I(t)$ versus the time delay obtained by reading the position of M2. From this graph, an estimation of τ (the laser pulse duration at FWHM, see Eq. 2.2) can be obtained from the FWHM of the autocorrelation trace τ_{AC}. Assuming that the pulse is Gaussian, a deconvolution factor of $\frac{1}{\sqrt{2}}$ has to be applied [11]:

$$\tau = \frac{1}{\sqrt{2}}\tau_{AC}. \tag{3.10}$$

Crosscorrelation

For achieving a cross correlation measurement, a reference beam significantly shorter than the pulse to characterize is needed, so that the reference pulse can be assimilated to a delta function and be used to sample the envelope of the pulse to characterize:

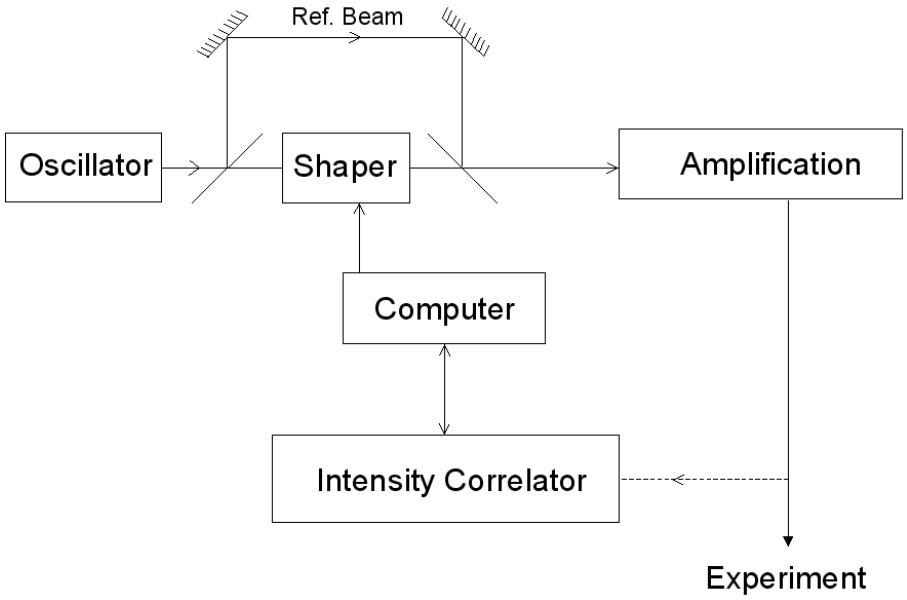

Figure 3.4: Overview of the building blocks for system I and system II

$$I_{AC} = \int_{-\infty}^{+\infty} I(t - \Delta t)\delta(t)dt. \tag{3.11}$$

The reference is obtained by deriving a fraction of the oscillator beam before spectral phase modulation, delayed by approximately 0.5 ns and amplified as shown in Fig. 3.4. The reference pulse is thus amplified on the same trail as the main pulse and preserves the quasi Fourier transformed characteristics. The amount of delay imposed to the reference pulse before amplification is strictly equal to $2d_{M2M'2}$ (see Fig. 3.4).

3.2 Beam manipulation for strong focusing in transparent materials

A femtosecond system has a unique ability for delivering energetic loads in a very short amount of time. The size of the beam is usually fixed to a value so that the energy density per pulse does not exceed the damage threshold of the optical elements used to guide the beam to the experiment. However, laser microprocessing of transparent dielectrics requires a high flux of photons so that nonlinear mechanisms can be triggered. Hence, the spatial confinement of the energy is extremely critical. Furthermore, strong focusing also implies a small beamsize in the focal region allowing a control of the laser action on scales down to the micrometer, promoting laser beams as flexible micromachining tools [60].

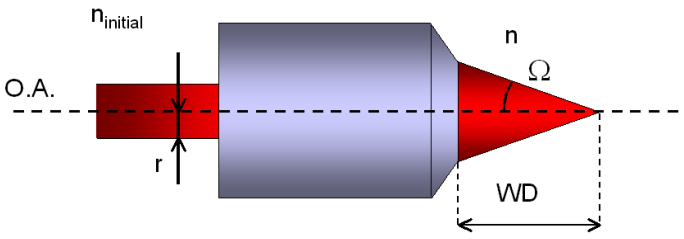

Figure 3.5: Figures of merit of a focusing system. The numerical aperture is simply defined as NA $= n \sin \Omega$. The working distance (WD), the radius of the back aperture (r) and the optical axis (O.A.) are also indicated.

3.2.1 Focusing of Gaussian beams

Figures of merit of a focusing system

The ability of an optical system to concentrate spatially an incoming electromagnetic vibration can be characterized in different ways. When focusing with a simple lens or simple optical systems, the usual relevant figure of merit is the focal length, f, defined as the distance between the focal point and the principal plane. When focusing with a microscope objective, f is usually not provided. Instead, manufacturers refer to the magnification and to the numerical aperture (NA). While the magnification is of little help regarding the focusing power of an optical system, the NA is a direct indicator defined as follows:

$$\mathrm{NA} = n \sin \Omega, \tag{3.12}$$

where n stands for the refractive index of the image space and Ω represents the angle of the steepest ray with respect to the optical axis, as depicted in Fig. 3.5.

As seen in Eq. 3.12, the maximum NA reachable in air is close to 1. Stronger focusing can be reached by using an immersion oil with a refractive index of typically 1.5. We underline that in the Eq. 3.12, the value of Ω depends on how well the back aperture of the focusing apparatus is filled. Hence, when focusing a laser beam with a microscope objective, a special care has to be taken in order to match the beam radius with the radius of the objective back aperture r. In the case of an investigation with the NA as a free parameter, this property can be used to decrease the NA by simple irisation of the incoming beam as suggested in [61].

Although the NA is a very convenient quantity, calculations require most of the time the focal length f as an input parameter. Therefore, it is of great help to consider an equivalent focal length f_{eq} defined as (see [61]):

$$f_{eq} = r\frac{\sqrt{n^2 - \mathrm{NA}^2}}{\mathrm{NA}}, \tag{3.13}$$

where r corresponds to the radius of the back aperture (see Fig. 3.13). In addition to the focusing power, the working distance (WD) of the focusing system as defined in Fig. 3.5 is also a critical parameter. For a microscope objective, the WD is defined as the distance between the output surface and the focal plane. For micromachining purposes, a long or super long working distance objective, respectively labeled LWD and SLWD on the housing, is highly beneficial as it leaves a comfortable free space between the focusing optics and the sample. As a drawback a LWD or SLWD implies a more extended output surface for the objective and therefore a bigger objective housing.

Spatial extent of a focused Gaussian beam

Under the action of a lens, in a uniform surrounding media, a monochromatic Gaussian beam with an initial radius w_0 is transformed into a Gaussian beam of radius w_f such as

$$w_f = \frac{f\lambda}{\pi w_0}, \tag{3.14}$$

f being the focal length of the focusing lens. The waist is commonly defined as the radius at which the intensity has fallen to $1/e^2$ with respect to its maximum value. Interestingly, as stated in [61], this previous result applies for focusing in any transparent medium, and does not scale with respect to n.

Along the direction of propagation, the collimation of a Gaussian beam can be estimated by the Rayleigh range z_r, defined as the distance from the plane of smallest radius to the plane at which the beam radius is larger by a factor of $\sqrt{2}$. In a general case, Rayleigh range and waist of a Gaussian beam w are related according to:

$$z_r = n\frac{\pi w^2}{\lambda} \tag{3.15}$$

Expressed as a function of NA, Eqs. 3.14 and 3.15 rewrite

$$z_r = \frac{\lambda}{\pi}\frac{1 - \mathrm{NA}^2}{\mathrm{NA}^2} \qquad and \qquad w_f = \frac{\lambda}{\pi}\frac{\sqrt{1 - \mathrm{NA}^2}}{\mathrm{NA}}. \tag{3.16}$$

It is then straightforward to get a first approximation of the focal volume simply by considering that the energy is enclosed in a cylindrical surface of radius w_f and of length $2z_f$.

The set of Eqs. 3.16 is only valid assuming that $w_0 = r$, i.e. the beam radius w_0 perfectly corresponds to r defined in Fig. 3.5 the so that Eq. 3.13 applies. However, it is experimentally difficult to warrant. Hence, the focal volume is sometimes estimated based on the intrinsic

characteristics of the focusing objective rather than from the initial beam waist [62]. For instance, one can use the radius of the first Airy disk to estimate the size of the focused beam. It follows that the radius of the focused beam w'_f is given by (see [30])

$$w'_f = \frac{0.61\lambda}{\mathrm{NA}}. \tag{3.17}$$

The axial extent of the beam, $2z'_r$, can be derived injecting Eq. 3.17 in Eq. 3.15:

$$2z'_r = 2n\frac{\pi w'^2_f}{\lambda}. \tag{3.18}$$

It is then easy to derive the expression of the focal volume V_{focal} and of the focal spot area S_{focal},

$$V_{focal} = \frac{0.947\lambda^3 n}{\mathrm{NA}^4} \qquad and \qquad S_{focal} = \frac{0.405\lambda^2}{\mathrm{NA}^2}. \tag{3.19}$$

3.2.2 Beam focusing in bulk materials: influence of spherical aberrations

The main difficulty to overcome in order to ensure efficient microprocessing of the bulk transparent materials relates to the presence of the interface between air and the transparent target during the beam propagation. The heart of the problem comes from the strong mismatch between the refractive indices of air and glass, introducing different optical paths for the different rays constituting the focusing cone upon refraction. This type of aberration is referred to as spherical aberration.

As a rule of thumb, the optical paths of peripheral rays are affected most. The major consequence is that the different propagating rays are brought at different locations on the propagation axis and cause a non negligible elongation of the focal region resulting in a intensity drop with the focusing depth. Nowadays, microscope objectives dedicated to biological observations are provided with adjustable collars so that spherical aberrations can be appreciably reduced when observing a specimen under a glass coverslip. Unfortunately, this feature is not systematically available. It appears that long working distance objectives convenient to use for dielectrics processing are originally designed for surface imaging in metallurgy applications, where a spherical aberrations correction collar is not desirable. Although the presence of spherical aberrations is unavoidable, it is of prime importance to be able to quantify their influence on the final on-axis intensity distribution.

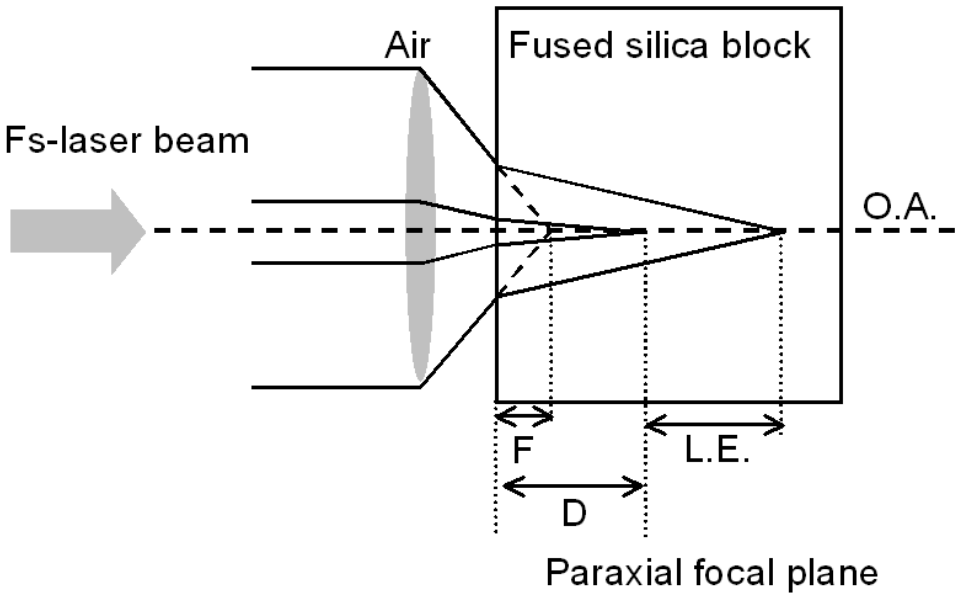

Figure 3.6: Experimental layout emphasizing the effect of spherical aberrations, adapted from [4]. The position of the paraxial focal plane with respect to the air-glass interface (D), the focal plane in absence of interface (F) and the longitudinal extent of the focal volume (L.E.) as well as the location of the optical axis (O.A.) are indicated.

Focusing through a plane interface: the wave plane solution

The general topic of focusing electromagnetic waves through a dielectric interface has triggered a considerable amount of theoretical efforts, see for instance [63] and references therein. Even though several methods have been proposed to address this question, the different approaches turn out to provide very similar solutions, as shown in [64]. Heeding the work of Hnatovsky and co-workers [4], the model developed in [63] is taken as a basis for simulating the consequences of spherical aberrations on the intensity distribution in the focal region. A scheme of the experimental layout taken from [4] is shown in Fig. 3.6.

This model is based on the theory of diffraction. The electromagnetic wave just before the air-dielectric interface is expressed as the sum of all the plane waves that can propagate within the cone of convergence defined by the numerical aperture of the objective. This sum is written as a superposition integral. Each plane wave is transmitted through the interface and brings a contribution to the transmitted field, again expressed as the superposition of every single transmitted plane wave. Since at the surface those two superposition integrals give the same field, the expression of the electric field in the dielectric medium can be written as [64]

$$E(z) = \frac{ik_1 f l_0}{2} \int_0^{\Omega} \sqrt{\cos\theta_1} \sin\theta_1 \exp\left[i(f-d)(k_1\cos\theta_1 - k_2\cos\theta_2)\right] \times (\tau_s + \tau_p \cos\theta_2) \exp(-ik_2 z \cos\theta_2) d\theta_1. \quad (3.20)$$

Ω is the semi aperture angle of the focusing objective (see Fig. 3.5), k_1 and k_2 are the wavevectors of the incident electromagnetic wave in air ($n_1 = 1$) and in the dielectric (refractive index n_2) defined as

$$k_1 = \frac{2\pi}{\lambda} \qquad and \qquad k_2 = \frac{2\pi n_2}{\lambda}, \quad (3.21)$$

l_0 is an amplitude factor, f is the focal length of the focusing system, τ_s and τ_p are the Fresnel transmission coefficients, respectively for a p-polarized and a s-polarized wave. After solving numerically Eq. 3.20, the intensity distribution in the focal region $I(z)$ along the propagation axis z can be easily computed using

$$I(z) \propto E(z)E(z)^*, \quad (3.22)$$

where $E(z)^*$ is the conjugated complex of $E(z)$. Following [64], an analysis of the different terms playing a role in the expression of the electric field on axis is of great interest. The part corresponding to the spherical aberration is written as a phase term causing distortion of the wavefront and is written as $\exp\left[i(f-d)(k_1\cos\theta_1 - k_2\cos\theta_2)\right]$. The factor $(\tau_s + \tau_p\cos\theta_2)$ is a polarization-dependent apodization function. The term $\exp(-ik_2 z\cos\theta_2)d\theta_1$ contains the defocus phase factor.

As a main limitation, this model does not take into account the response of the material to the external electromagnetic excitation. The nonlinear response of the target and all absorption phenomena are ignored. This aspect can not be discussed with such a model and requires a more advanced modeling scheme.

Numerical results

The integral giving the expression of the electric field on axis (see Eq. 3.20) does not have analytical solution. Hence, we need to search for an approximate numerical solution of this integral for each point on the z axis. The numerical integration of Eq. 3.20 has been performed with Matlab 7.1.0.246. Among the different integration functions available, `quadl`, based on adaptive Lobatto quadrature, has been preferred to methods employing simple Simpson quadrature. The parameters used to compute the integral in Eq. 3.20 correspond to the experimental conditions when focusing a monochromatic source of light with a wavelength of $\lambda = 800$ nm with a microscope objective (NA=0.45, back aperture radius = 2 mm)

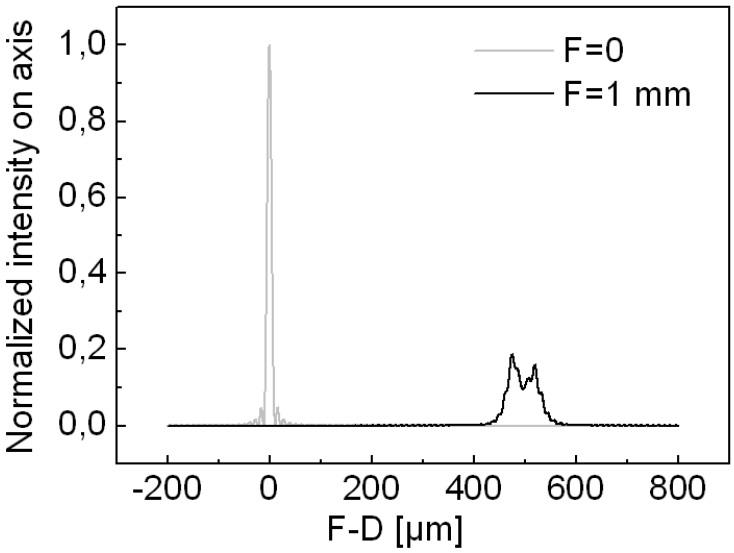

Figure 3.7: On axis intensity distribution generated by spherical wavefront distortion for $F = 0$ and $F = 1$mm. F and D correspond to the position of the focal plane in absence and in presence of a air-glass interface, respectively (see Fig. 3.6).

in pure amorphous fused silica ($n = 1.453$). Results are plotted on Fig. 3.7, for two different focusing depths $F = 0$ and $F = 1$ mm. We remind that F and D correspond to the location of the paraxial focus in absence and in presence of a air-glass interface, respectively (see Fig. 3.6).

The case $F = 0$ corresponds to focusing on the air-glass interface. Therefore, spherical aberrations do not play any role in this case. The electric field is essentially confined to a 10 μm full width at half maximum peak, centered at $F = 0$. Some lobes can be seen on each side of the peak, in good agreement with the results given by the theory of diffraction for the light distribution on axis in the focal region of a lens. The detailed calculations can be found for instance in [30] p. 491, and provide the following analytical expression for the electric field:

$$I(z) = I_0(\frac{\sin(z/4)}{z/4})^2 \tag{3.23}$$

where I_0 is an amplitude factor. When $F = 1$ mm, the electric field distribution on axis is substantially affected. Three striking features are worth being underlined from Fig. 3.7. Firstly the whole focal volume is translated deeper in the bulk. The field distribution is approximately centered around a position corresponding to the paraxial focal plane in presence of an interface [4], at a distance D from the interface such as

$$D = F\frac{n_2}{n_1}. \tag{3.24}$$

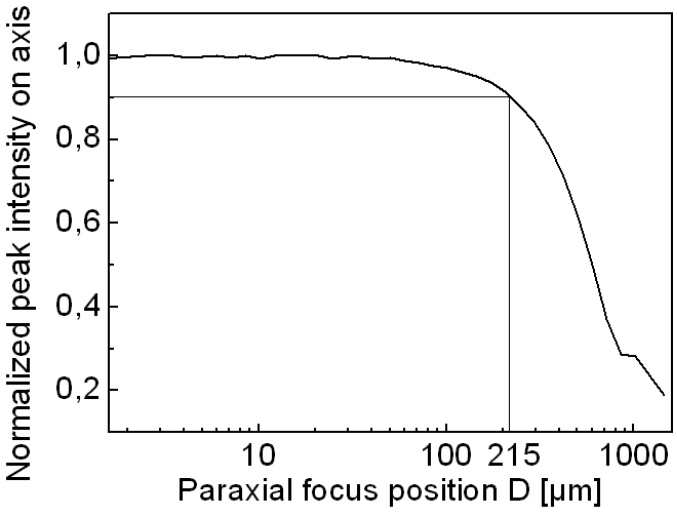

Figure 3.8: Intensity peak on axis when varying the position of the paraxial focus (D) in presence of an air-glass interface.

Secondly the spatial extent of the electric field on-axis dramatically increases as the focusing depth increases, and is accompanied by a reduction in magnitude in good agreement with experimental observations reported in [4] or [65]. Finally, a multipeak structure appears and the maximum intensity of the electric field on axis drops dramatically. In order to estimate at which depth D into the material the spot can be focused without experiencing significant modifications, the integral in Eq. 3.20 is solved for different values of D. The maximum value of $I(z)$ is extracted for each focusing depth and is plot as a function of D. Results are shown in Fig. 3.8. The parameters for the integration are the same as for Fig. 3.7. For a NA=0.45, the maximum intensity on axis stays within 90% of its maximum value for focusing depths D_{max} up to 215 μm. Experimentally, a special care is taken so that $D < D_{max}$ in order to work in conditions where the influence of the air-glass interface is minimized.

3.3 Fundamentals of phase contrast microscopy

3.3.1 Overview of refractive index change detection methods

The analysis of laser-induced modifications in the bulk of transparent materials is a delicate topic. The difficulty does not arise from the size of the photowritten objects but from their transparency, making them almost or totally invisible to traditional microscopy techniques. When a moderate laser energy is used, the target material is able to stand the transfered

energetic load without experiencing major damage such as cracking. If the input energy exceeds the threshold for material modification without provoking material cracking, the laser processing only alters the real part of the refractive index and results in the onset of a pure phase object. Such a phase object is differentiated from its surrounding bulk by a slightly different refractive index. The amplitude of the refractive index difference Δn is typically of less than a percent. Several techniques have proven their efficiency to characterize such objects. Some groups notably reported quantitative estimations using cleaving and electronic microscopy [66], etching [49, 67], refracted-near-field profilometry [68] or digital holography microscopy [69]. As a main drawback, all of those methods are time-consuming and necessitate post processing of the sample.

Overcoming those major disadvantages, Yamada *et al.* [70] reported *in-situ* observations of laser-induced phase objects with three different apparatus. A polarization sensitive method (Sénarmont compensator), a coherent filtering method based on a Schlieren arrangement and a focusing method [71] were successively used to gather quantitative informations about the amplitude of refractive index change in filaments formed in glasses by femtosecond laser pulses. The focusing method is based on an analysis of the transmitted light trough the sample and requires a step of post calculations. This technique relies on the fact that a refractive index gradient has observable and measurable consequences on the propagation of a coherent wavefield.

Following this idea, a remarkable method called quantitative phase microscopy (QPM) has been developed [72] and commercialized. QPM is able to provide a 2-dimensional map of the refractive index distribution in an arbitrary plane of the considered sample with quantitative estimations of the refractive index change. By using a suitable imaging system as a microscope, the spatial resolution can be pushed to the limits of diffractive optics. QPM is based on the post analysis of two slightly out-of-focus images taken in the planes P_1 and P_2, those planes being located symmetrically at each side of the main focus. Typically, the distance between P_1 and P_2 is of a few μm. By solving the intensity transport equation, it is possible to determine the refractive index profile of the propagating medium in between P_1 and P_2. Those steps of calculations are unfortunately not acceptable with respect to our need for an instantaneous phase map visualization. Thus, our choice goes to either a polarization-sensitive technique or a coherent filtering method. In order to obtain a satisfying spatial resolution, the choice is restricted to either differential interference contrast (DIC) microscopy or phase contrast microscopy (PCM).

A detailed comparison of DIC with PCM is available on the Internet[6]. As a main disadvantage, a halo shows up around big size objects visualized in PCM. To its advantage, PCM exhibits a higher sensitivity compared to DIC microscopy, which is based on refractive

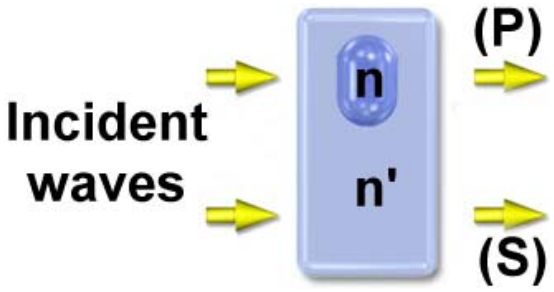

Figure 3.9: Principles of optical phase contrast microscopy. Adapted from [5]. Sketch of the object to study. The surround (S) wave and and a wave emerging from the object (P) are schematically represented.

index gradients imaging. Furthermore, phase contrast microscopes do not comprehend thick optical elements, contrary to DIC microscopes in which a pair of prisms is inevitably used. As this feature is likely to play an important role for the time-resolved studies described in Ch. 5, it is decisive in the choice of employing a phase contrast microscopy method for our investigations.

3.3.2 Qualitative study of the phase contrast technique

Case of pure phase objects [73, 74, 6, 5]

Let us consider the general case where the specimen to study is a small transparent object with a refractive index n embedded in a transparent bulk of refractive index n' such that $n > n'$ (see Fig. 3.9).

In such a configuration, rays of light propagating through the object, like ray (P) are slightly delayed with respect to the ones crossing the surrounding homogeneous medium, such as ray (S), due to a difference in their respective optical paths. If it is assumed that those rays of light are monochromatic, it is possible to associate to each of them a sinusoidal vibration (Fig. 3.10) of equal amplitude a, as we stated that the dephasing object is transparent.

The temporal delay experienced by ray (P) simply translates in terms of a small phase difference, represented by a small shift along the space axis toward the left side. Interestingly, the representative curve of ray (P) can be decomposed into the sum of a wave emerging from the background (S) with a diffracted wave, referred to as (D) on Fig. 3.10.

Obviously, the diffracted wave (D) carries the information about the object being studied. Hence, it is of primary importance to maximize the contribution of this wave to the final image formation. Basically, the intensity resulting from the superposition of wave (S) and (D) is

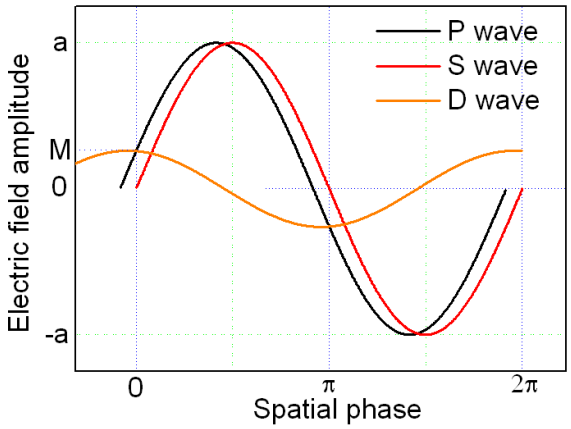

Figure 3.10: Representative curves of the electric fields of the surrounding (S), particle (P) and diffracted (D) waves.

$$I_{object} \propto |E_{sum}|^2 = E_{sum}E^*_{sum}, \tag{3.25}$$

where

$$E_{sum} = E_P = E_S + E_D = a\exp(j\omega t) + O\bar{M}\exp(j\omega t + \varphi). \tag{3.26}$$

In this last equation, a and $O\bar{M}$ represent the amplitudes of waves (S) and (D), ω is their pulsation, and φ their relative dephasing. In Eq. 3.31, E^*_{sum} stands for the conjugated complex of E_{sum}. By combining Eq. 3.26 and Eq. 3.31, one obtains

$$I_{object} \propto a^2 + 2aO\bar{M}cos\varphi + O\bar{M}^2. \tag{3.27}$$

Waves coming from the surrounding bulk give a uniform intensity I_{bkg} in the image plane such as

$$I_{bkg} \propto a^2. \tag{3.28}$$

When the sample is studied in normal microscopy, the object naturally provokes $\varphi = \frac{\pi}{2}$ for wave (D), as shown in Fig. 3.10. In this case, Eq. 3.27 reads

$$I_{object} \propto a^2 + O\bar{M}^2. \tag{3.29}$$

If the shift between waves (P) and (S) is small *i.e.* if n and n' are close, $O\bar{M}$ is also small. Hence, Eq. 3.29 reduces to

$$I_{object} \propto a^2 \tag{3.30}$$

and waves emerging from the object bring the very same contribution to the final image as the direct waves coming from the rest of the bulk. The intensity is then uniform on the

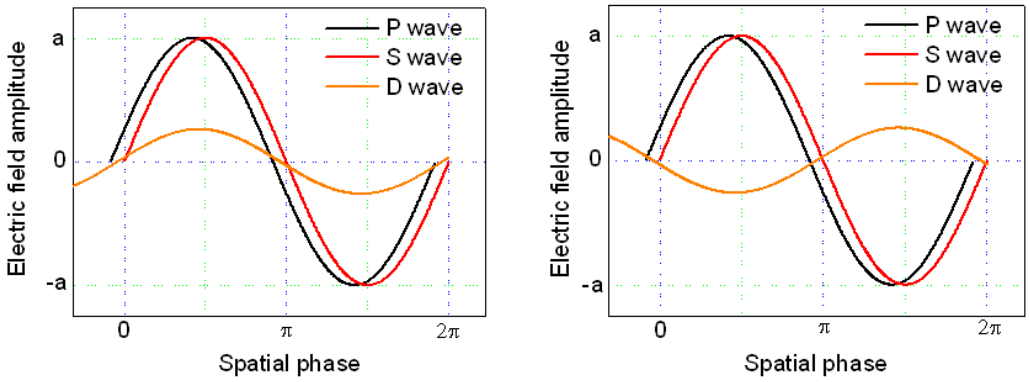

Figure 3.11: Artificial shift of the diffracted wave by $+\frac{\pi}{2}$ (left) or $-\frac{\pi}{2}$ (right).

whole image plane and the transparent object remains invisible. In order to maximize the contribution of wave (D) it is of great benefit to shift it by an additional $\varphi_{artificial} = \pm\frac{\pi}{2}$ with respect to wave (S), as shown in Fig. 3.11. Equation 3.27 can then be rewritten:

$$I_{object} \propto a^2 \pm 2aO\bar{M}, \tag{3.31}$$

as $O\bar{M}^2$ is still negligible. In the image plane, the direct waves emerging from the undisturbed bulk remain the same as before. Hence, by setting artificially an additional phase shift of $\varphi_{artificial} = \pm\frac{\pi}{2}$, $I_{object} \neq I_{bkg}$ and the object becomes visible. If $\varphi_{artificial} = +\frac{\pi}{2}$, $I_{object} < I_{bkg}$ and the object of higher refractive index appears darker than the background. This case corresponds to positive phase contrast microscopy. Inversely, in a negative phase contrast setup, a negative additional phase shift is added to wave (D) and an object of higher refractive index appears brighter than the background. In a negative phase contrast microscopy setup, the contrast C can be written as

$$C = |\frac{I_{bkg} - I_{object}}{I_{bkg} + I_{object}}| = |\frac{a^2 - a^2 + 2aO\bar{M}}{a^2 + a^2 - 2aO\bar{M}}| = |\frac{O\bar{M}}{a - O\bar{M}}| \tag{3.32}$$

According to this definition, $0 < C < 1$. The smaller a, the higher the contrast. Hence, in addition to an artificial dephasing of wave (D) with respect to wave (S), an attenuation of wave (S) is highly profitable to the contrast. Those two features are the angular stone of phase contrast microscopy.

Case of non transparent objects

If the observed object is not transparent, waves crossing the object should then be decomposed as the sum of a direct wave (S') and a diffracted wave (D'). The amplitudes of (S') and (D') write respectively

$$O\bar{M}' = (1 - \zeta)O\bar{M} \tag{3.33}$$

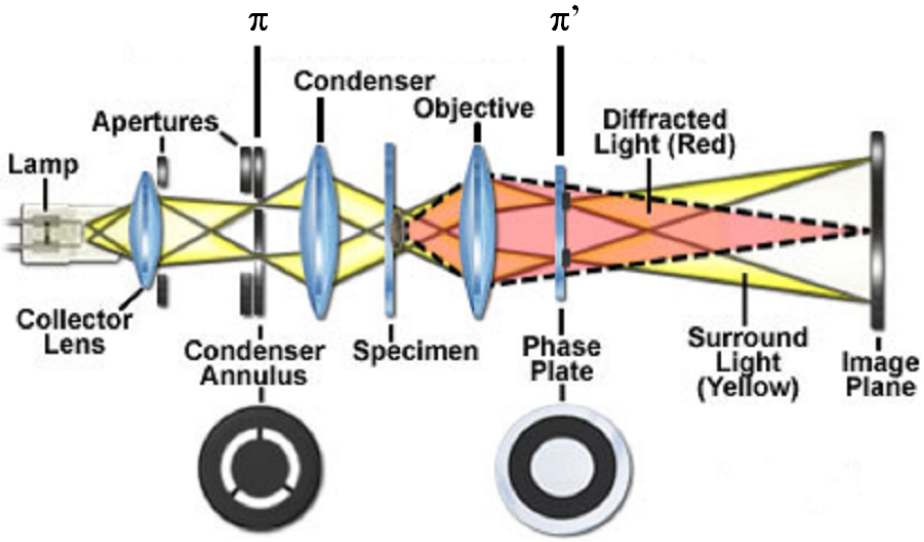

Figure 3.12: Phase contrast microscope optical train, taken from [6]

and

$$a' = (1 - \zeta)a, \tag{3.34}$$

where $(1 - \zeta)$ is the ratio of transmitted fields through the object.

In a similar way to Eq. 3.31 the intensity of the object recorded in a phase contrast arrangement now writes:

$$I_{object} \propto a'^2 \pm 2a'O\bar{M}' = (1 - \zeta)^2 a^2 - 2(1 - \zeta)^2 aO\bar{M}, \tag{3.35}$$

where a corresponds to the amplitude of the unattenuated wave through the bulk. The two coefficients a and ζ can be retrieved from traditional transmission microscopy measurements. The intensity corrected from absorption I_{cfa} of the phase object from a transmission then writes

$$I_{cfa} \propto a^2 \pm a^2 - \frac{I_{object}}{(1 - \zeta)^2}, \tag{3.36}$$

for negative and positive phase contrast apparatus, respectively.

3.3.3 Practical realization

The optical train of a phase contrast microscope is shown in Fig. 3.12. This optical train is very similar to the one of a classical microscope (see for instance [73]) with the addition of a condenser annulus and a phase plate. The object, referred to as "specimen" on Fig. 3.12, is illuminated by the lamp and diffracts a small portion of incident light in a cone represented in red, while the yellow parts of the light train correspond to the normal trajectory of light

without specimen. The smaller the specimen, the wider the red cone. Interestingly the diffracted light and the direct light are clearly discriminated in the focal plane (π') of the objective. Hence, it is easy to act selectively on the direct or diffracted light in this plane. This is logically where the dephasing and attenuation of the direct light is done by an element called phase plate. The image of the focal plane of the condenser (π) through the system $\{condenser + objective\}$ is located at the focal plane of the objective π'. It implies that the phase plate and the diaphragm are also conjugated. A ring-shaped diaphragm is commonly used, as shown in Fig. 3.12. Practically, this diaphragm is located a few millimeters in front of the condenser, and is simply made of a dark absorbent plastic sheet with an annular opening. The phase ring is generally inserted into the objective, and visible by direct looking. This feature is generally labelled P* or N* on the outer housing of the objective. The letter P or N indicates whether the phase plate will delay the direct light (negative phase contrast, labelled N, regions with higher refractive index appear lighter) or the diffracted light (positive phase contrast, labelled P, the regions of higher refractive index appear darker). The letters following refer to the absorption factor of the wave plate, and can take the value LL, L, M, H corresponding to respectively Low Low, Low, Medium and High (see [5] for further details). "Low" stands for low contrast and "High" for high contrast.

Although Eq. 3.32 suggests that the higher the absorption the better the contrast, practical considerations developed in [73] render difficult the use of a phase plate with an attenuation coefficient higher than 50 times. Nevertheless, in those conditions, variations of the optical path of a few Angströms only are detectable.

3.4 Experimental setup

The main building blocks presented here are used as a basis all along this thesis, with some variations depending on the specificity of the task to accomplish. Because each device plays a crucial role in the experimental success, details on the manufacturer and on the references are provided when possible.

3.4.1 Pulse picking

At the output of the laser, we use an electro-mechanical shutter commercialized by Uniblitz. Depending on the diameter of the laser beam, the models LS6 or VS14 (for a larger aperture) have been employed. The opening and closing times increase with the size of the aperture and define the maximum repetition rate of the source allowing single pulse picking. For the LS6, the maximum repetition rate of the laser source is of about 400 Hz whereas for the

VS14, it is limited to 154 Hz. The shutter opening is triggered by the output of the Pockels cell. The signal corresponding to the delivery of a pulse N is electronically delayed in order to synchronize the shutter aperture with the arrival of the pulse N+1. The electronic delay is carefully set with the help of an ultrafast photodiode placed behind the shutter.

3.4.2 Beam focusing

A microscope objective is used in order to confine spatially the laser beam. A challenge is to find a microscope objective capable of strong focusing but also providing a comfortable working distance. This latter property allows one to simultaneously write and observe the results under the phase contrast microscope. For this purpose, we exclusively use a super long working distance objective manufactured by Nikon. The working distance (see Fig. 3.5) is of 17 mm. The numerical aperture of 0.45 corresponds to a compromise. Higher numerical aperture devices do not offer the possibility to have a long working distance and low numerical aperture objectives are not suitable for applications such as transverse waveguide writing, because the volume of interaction with the target material is considerably elongated along the propagation axis. This results in a strong ellipticity of the laser generated structures. As a drawback, our objective is originally designed for observations on the surface and is not corrected for spherical aberration. Special attention has been paid to the control of the focusing depth in the bulk for working under a configuration where the influence of the spherical aberrations is significantly attenuated, as discussed in Sec. 3.2.2.

3.4.3 Samples and sample displacement

Our samples are parallelepipeds of $3 \times 20 \times 10$ mm polished on the 4 faces of greater area. The present studies are carried out on two different glasses, pure amorphous silica (a-SiO_2) and N-BK7. BK7 is a borosilicate crown glass manufactured by Schott, widely used as technical optical glass for applications in the visible region. The chemical composition of BK7 as specified by Schott in percentage by weight is the following: silica(70-80), boron oxide(10-20), sodium oxide (1-10), potassium oxide(1-10), barium oxide(1-10), titanium oxide, calcium oxide and antimony trioxide in small quantities (less than 1 percent). Samples are fixed on a homemade sample holder mounted on two motorized translation stages (Physik Instrumente model M-126.DG) in the horizontal plane while the vertical positioning is ensured by a manual translation stage. The motorized stages are connected to a PC and are compatible with LabView. They allow a positioning of the sample with a precision better than 1 μm.

3.4.4 Phase contrast apparatus

The microscope used for the characterization of the irradiated samples in transmission is an Olympus BX-41. The phase contrast investigations are achieved by simple adjunction of a phase contrast module. For the observation, we use positive-high (Ph) phase contrast objectives (20x, 40x, and 60x). According to Sec. 3.3.2, this means that an object with a higher refractive index than the surrounding bulk appears darker than the background. The recording of the microscope images is made with a Jai camera model CV-A1. The CCD matrix is made of 1392 $\times$ 1040 square pixels. The size of the pixel is of 4.65 μm. The camera is connected and driven by a PC and is compatible with LabView.